Collectivity at high spins in ^{156}Dy

P. Petkov,[1,2] A. Dewald,[1] O. Möller,[1] B. Saha,[1] A. Fitzler,[1] K. Jessen,[1] D. Tonev,[1] T. Klug,[1] S. Heinze,[1] J. Jolie,[1] P. von Brentano,[1] D. Bazzacco,[3] C. Ur,[3] E. Farnea,[3,4] M. Axiotis,[4] S. Lunardi,[3] C. Rossi-Alvarez,[3] G. de Angelis,[4] D. R. Napoli,[4] N. Marginean,[4] T. Martinez,[4] M. Caprio,[5] and R. F. Casten[5]

[1]*Institut für Kernphysik der Universität zu Köln, 50937 Köln, Germany*

[2]*Bulgarian Academy of Sciences, Institute for Nuclear Research and Nuclear Energy, 1784 Sofia, Bulgaria*

[3]*Dipartimento di Fisica and INFN, Sezione di Padova, Padova, Italy*

[4]*INFN, Laboratori Nazionali di Legnaro, Legnaro, Italy*

[5]*Wright Nuclear Structure Laboratory, Yale University, New Haven, Connecticut, USA*

(Received 8 May 2003; published 29 September 2003)

Mean lifetimes of five levels in the *S* band and three levels in the ground-state band of ^{156}Dy, populated via the ^{124}Sn(^{36}S,$4n$) reaction at $E=145$ MeV, were measured by the Doppler-shift attenuation technique using a line-shape analysis. The differential decay-curve method was applied for a lifetime determination. In contrast with earlier data, the present $B(E2)$ values in the yrast band do not indicate a reduction in the collectivity after the crossing between the *S* band and the ground-state band, and confirm the results of theoretical calculations using mean-field approaches.

DOI: 10.1103/PhysRevC.68.034328 PACS number(s): 21.10.Tg, 23.20.Lv, 27.70.+q

I. INTRODUCTION

Numerous experimental and theoretical investigations have been dedicated to ^{156}Dy over the past decades. Lying in a transitional region between spherical and deformed nuclei, this nucleus is a natural laboratory for the experimental revelation of a large variety of phenomena and a challenging testing ground for theoretical models. The high-spin studies of ^{156}Dy yielded a wealth of information about the interplay between collective and single-particle degrees of freedom. The near yrast discrete line γ-ray spectroscopy [1] established numerous band structures in this nucleus. Ten years later, the discrete normal deformed states with highest spins ($I\approx 60\hbar$) observed so far were investigated in Ref. [2] where a smooth prolate to a noncollective oblate shape evolution was suggested for the lowest bands with positive parity ($\pi=+$). The yrast states have been an object of investigation already since the early 1970s. The works of Andrews *et al.* [3] and Lieder *et al.* [4] pointed out the interesting phenomenon of the crossing between the β band and the *S* band, with the latter becoming yrast at the $I^{\pi}=16^{+}$ level, where the levels of the continuation of the ground-state band (g.s.b.) start to form the yrare sequence. A portion of the high-spin level scheme of ^{156}Dy is presented in Fig. 1. The lifetimes of the yrast states up to high spins were determined in a series of experiments by Ward *et al.* [6] and Emling *et al.* [7,8]. The results of Refs. [7,8], where individual lifetimes of levels of the *S* band above $I^{\pi}=20^{+}$ have been measured, implied rotationally induced shape changes affecting the parameters β and γ of the intrinsic quadrupole deformation. These changes led to a reduction of the collectivity, expressed through the $B(E2)$ values, already in the spin region $I^{\pi}=22^{+}-30^{+}$ in comparison with what is observed at lower spins. In this spin region, the structure of the yrast band is dominated by two unpaired $i_{13/2}$ quasineutrons, and only at higher spins additional quasiparticles successively align and finally make the collectivity vanish at the band-terminating state. The purpose of the present work is to remeasure the lifetimes of the levels in the spin region $I^{\pi}=22^{+}-30^{+}$ using the Doppler-shift attenuation method (DSAM) [9] and to verify the earlier suggested drop in the $B(E2)$ values. One of the reasons for this is the fact that many theoretical calculations using mean-field approaches, e.g., Refs. [10–12], do not predict such a significant reduction of the collectivity in the spin region considered. Apart from the interesting physical topic, our work has been additionally motivated by the advances of the experimental techniques, which make possible nowadays the use of large multidetector arrays and provide the analysis with data of higher statistics.

II. EXPERIMENT

The excited states of interest in ^{156}Dy were populated using the reaction ^{124}Sn (^{36}S, $4n$) at an energy of 145 MeV with a beam provided by the XTU tandem of the Laboratori Nazionali di Legnaro, Italy. The target consisted of a 0.9 mg/cm^2 Sn foil enriched to 95.3% in ^{124}Sn. It was evaporated onto a 13.4 mg/cm^2 Ta foil serving as a backing to stop the recoils which were leaving the target with a mean velocity of about 1.83% of the velocity of light, *c*. The γ rays deexciting the recoiling ^{156}Dy nuclei, which are produced in the dominating exit channel of the reaction, were registered with the GASP array [13] in configuration I. This array consists of 40 large volume Compton suppressed germanium detectors which can be grouped in to seven rings for the data analysis. The detectors of each ring are positioned at approximately the same angle θ with respect to the beam axis, namely, ring 0 ($\theta=34.6°$), ring 1 (59.4°), ring 2 (72°), ring 3 (90°), ring 4 (108°), ring 5 (120.6°), and ring 6 (145.4°). For the present DSAM experiment, the rings of main interest are these where appreciable Doppler shifts can be observed, i.e., rings 0, 1, 5, and 6. Each of these rings consists of six detectors. The trigger condition for data acquisition was set to the registration of at least two germanium signals firing in prompt coincidence. About 0.7×10^9 unfolded doubles

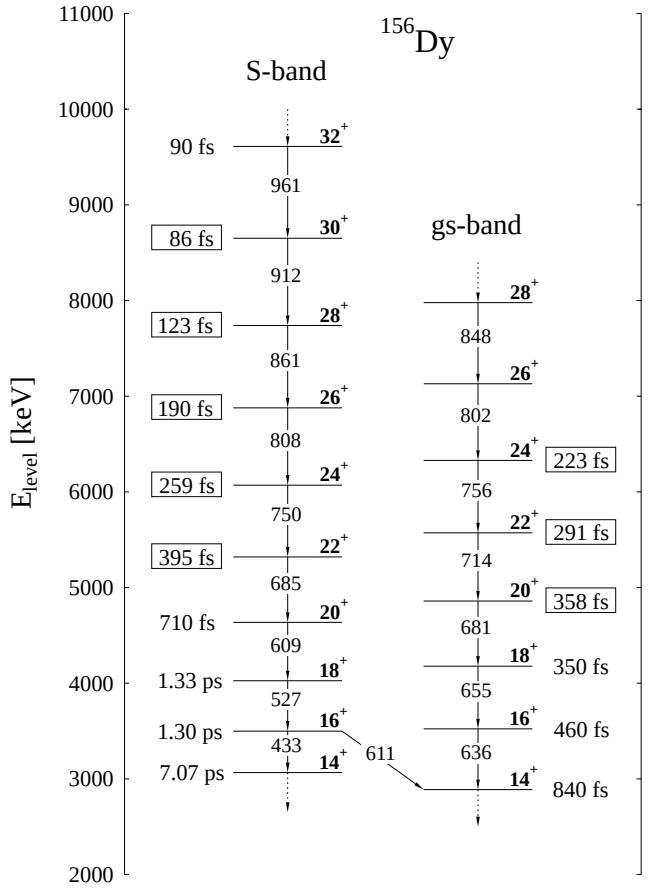

FIG. 1. Partial level scheme of ^{156}Dy according to Ref. [5]. Lifetimes determined in the present work are displayed in solid framed boxes. Additional available lifetime information [5] is also shown.

events were collected in the measurement. After corrections for energy shifts and energy matching of the detectors, the data were initially sorted out into two groups of 49 $4k \times 4k$ γ-γ coincidence matrices, where each matrix accumulates events corresponding to the registration of two γ rays by the detectors belonging to a particular pair of rings of the GASP. The first group of matrices was built using a window set on the prompt time peak, while the time window for the second group was set away from this peak on a background region where the random coincidences dominate. To correct for the latter, the matrices of the second group were subtracted from the corresponding matrices of the first group. Then, gates were set in the resulting matrices in order to check if the quality of the gated spectra allows for a DSA analysis which eliminates the problem of the unknown or side feeding of the level of interest. Our recently published procedures solve this problem for a pair of two subsequent γ rays, with a gate on the Doppler-shifted fraction of the feeding transition [14] or with a gate on any fraction of the depopulating transition [15]. Unfortunately, the statistics turned out to insufficient for the application of these two approaches. Therefore, we have built a set of four new γ-γ matrices, with one of their axes corresponding to the detection of a γ ray in ring 0, 1, 5, and 6, respectively, whereas the

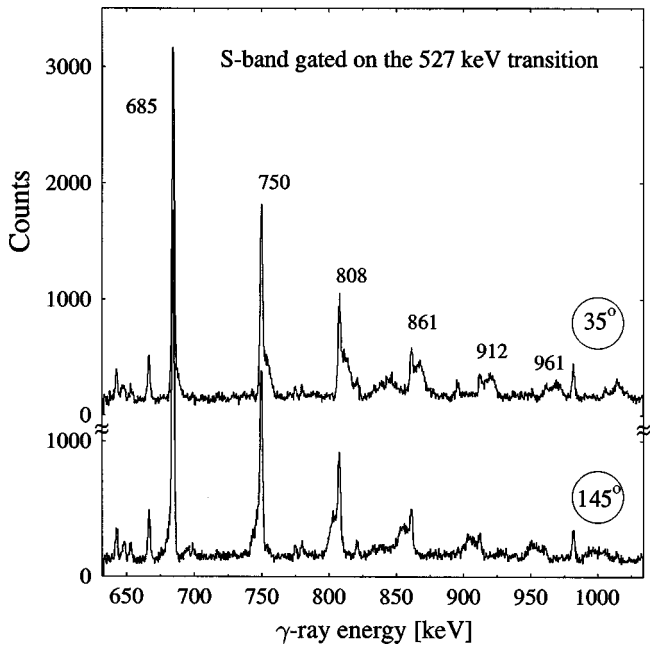

FIG. 2. Line shapes of transitions in the *S* band of ^{156}Dy obtained with a gate set on the 527 keV transition at all seven rings of the GASP. The spectra are measured with the detectors positioned at 35° (ring 0) and 145° (ring 6) with respect to the beam axis. The energies of the γ-ray transitions are indicated in keV.

other axis being associated with a detection of the second coincident γ ray in any ring of the GASP. Spectra for further analysis were generated by setting gates at the latter axis on fully stopped peaks of lower-lying transitions, i.e., ''from below.'' Examples of such spectra, showing transitions in the *S* band of ^{156}Dy, are displayed in Fig. 2 to illustrate the quality of the data. In addition, a matrix was built which accounts for the full statistics of the experiment by accumulating γ-γ coincidences between any pair of rings of the GASP. This matrix served to obtain information on the intensities of the γ rays of ^{156}Dy observed in the experiment. As a part of the experiment, energy, full width at half maximum, and efficiency calibrations were made with a ^{152}Eu source. With the same setup, we performed also a recoil distance Doppler-shift (RDDS) lifetime measurement, the results of which will be presented and discussed in a forthcoming paper [16].

III. DATA ANALYSIS

The slowing down of the recoiling nucleus in a material and the decay of its excited states occur independently, but being initiated by the same nuclear reaction, they are correlated in time. This fact is the basis of the well established DSAM for lifetime determination (cf., e.g., Ref. [9]). Experimentally, the method is realized by measuring the spectrum of γ rays at a given direction of observation, e.g., at an angle θ with respect to the beam axis. The Doppler-shift formula $E'_\gamma = E_{\gamma_0}(1+v_\theta/c)$ describes the relation between the precise registered energy E'_γ, the energy of the γ ray emitted at rest E_{γ_0}, and the recoil velocity projections v_θ on this direction, and thus correlates the decay and slowing-down histo-

TABLE I. Parameters of the electron stopping power [Eq. (2)]. See also text.

^{156}Dy ions	Upper energy limit (MeV)	f_e	a
Sn (enriched to 95.3% in ^{124}Sn)	26	0.844	0.643
Ta	11	0.543	0.631

ries. After taking into account the response function Φ of the detector, the measured singles spectrum or line shape is given by

$$S_{ij}^{\gamma}(E_{\gamma}) = \int_{-\infty}^{\infty} dE'_{\gamma} \frac{c}{E_{\gamma_0}} \Phi(E'_{\gamma}, E_{\gamma}) \times \int_0^{\infty} dt P_{\theta}(t, v_{\theta}(E'_{\gamma})) b_{ij} \lambda_i n_i(t). \quad (1)$$

Here, quantity $n_i(t)$ represents the population of level i as a function of time t, λ_i is the decay constant of that level and b_{ij} is the branching of the deexciting transition $i \rightarrow j$ under investigation. The stopping matrix $P_{\theta}(t, v_{\theta})$ represents the normalized distributions of the velocity projection v_{θ} at different times t. Depending on the experimental situation, additional corrections for geometry, efficiency, angular correlation, and kinematics effects (cf. Ref. [9]) have also to be taken into account in Eq. (1).

Our approach for analyzing DSA line shapes and deriving lifetimes is thoroughly presented in Refs. [17,18]. Referring the reader for more details to these papers, here we only remind the main points and concentrate on features specific to the present work. In this section, we discuss (i) the determination of the stopping matrix $P_{\theta}(t, v_{\theta})$ to describe the stopping process; (ii) the line-shape analysis, i.e., the solving of Eq. (1) with respect to the decay function $b_{ij}\lambda_i n_i(t)$ of the transition $i \rightarrow j$; and (iii) extraction of the lifetime $\tau_i = 1/\lambda_i$ of the level of interest, i, whereby the influence of the higher-lying feeding levels has also to be taken into account. As an illustration, we use the case of the transition of 808 keV which depopulates the $I^{\pi} = 26^+$ level in the S band (cf. Fig. 1). The results obtained in this band as well as in the ground-state band are presented in the following section (Sec. IV).

For the description of the stopping process, i.e., for the calculation of the matrix $P_{\theta}(t, v_{\theta})$ in Eq. (1), we used a modified version of the computer code DESASTOP [19,20] by Winter. This version allows for a numerical treatment of the electron stopping powers at relatively higher ion energies, where a simple expression such as the generalization [21] of the formula following from the Lindhard, Scharff, and Schiøtt (LSS) theory [22]

$$\left(\frac{d\epsilon}{d\rho}\right)_e = f_e k_{LSS} \epsilon^a \quad (2)$$

is not anymore valid. We recall that Eq. (2) describes the electron stopping power in terms of the dimensionless variables of the LSS theory, where k_{LSS} is a theoretical constant while f_e and a are fitting parameters ($a_{LSS} = 0.5$, $f_e^{LSS} = 1.0$, and ϵ is proportional to the kinetic energy of the ion and ρ to the distance). Our new version of DESASTOP [19,20] uses this equation only at low ion energies, below some limiting value, where its right-hand side is fitted to the numerical data. The numerical electron stopping power for ^{156}Dy in the target and stopper materials were determined from tabulated data as follows. First, the electron stopping power for ^{164}Dy ions in Sn (Ta) was interpolated (taken) from the semi-empirical tables of Northcliffe and Schilling (NS) [23] and converted into stopping power for ^{156}Dy ions by a correction for the mass difference. An additional correction was made for the details of the atomic structure of the medium using Refs. [24,25] which account for deviations from the relatively smooth dependence on Z predicted by the NS tables [23]. To adjust the electron stopping power of the Sn target, we used the above mentioned accompanying RDDS measurement [16], namely, the positions and widths of the Doppler-shifted γ-ray peaks at large target-to-stopper distances. Finally, the data were transformed in LSS units and fitted with the function on the rhs of Eq. (2). The derived parameters f_e and a are presented in Table I. The nuclear stopping power, which is due to the interaction with the atoms of the medium as a whole, was taken into account in our code according to the LSS theory [22] and the parametrization of the universal scattering function for a Thomas-Fermi potential given in Ref. [21]. To correct for the effect of microchanneling in the stopping medium, the nuclear stopping power was reduced by a factor $f_n = 0.7$ (cf. Refs. [26,24] for more details). The successful use, in the past [18], of the procedure described above make us confident of the reliability of the stopping powers employed in the present work. Nevertheless, we have also investigated (cf. below) the effect of deviations of 10% in these quantities on the derived lifetimes. According to our calculation, the distribution of the stopping times of the ^{156}Dy recoils is characterized by a mean value of 1.24 ps and a variance of about 0.25 ps. These values set upper limits for the effective lifetimes (feeding time plus own lifetime) of the levels accessible for the DSA analysis in the present study. Finally, it should be mentioned that our code follows closely the Monte Carlo calculation of the stopping process proposed by Currie [21]. However, additional randomizations, which take into account the effects of the reaction kinematics and the finite size of the detectors, are also performed.

In order to obtain the line shapes of the investigated γ-ray transitions in the S band and g.s.b. of ^{156}Dy, as already mentioned, gates were set in the γ-γ coincidence matrices on fully stopped peaks of lower-lying γ-ray transitions. Then, the gated spectra were inspected for their cleanness, with the requirement for consistent line shapes at forward and backward angles. The best spectra, used in the subsequent analysis, were generated with gates set on the 527- and 636-keV

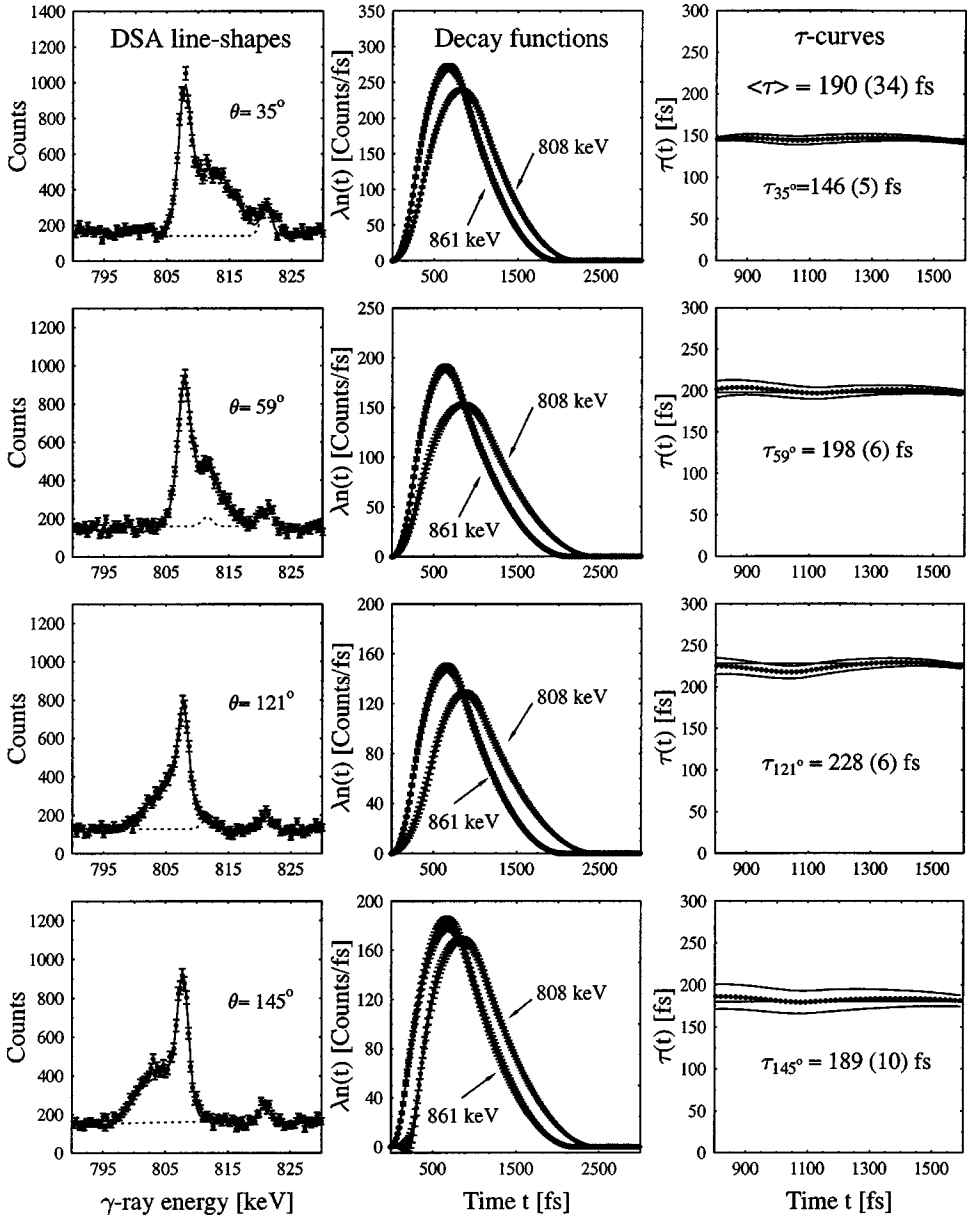

FIG. 3. Line shape analysis of the 808-keV transition in the *S*-band and determination of the lifetime of the $I^{\pi}=26^{+}$ level at 6878-keV according to the DDCM [cf. Eq. 3]. On the left-hand side are shown fits of the lineshapes measured at the angles of 35°, 59°, 121°, and 145° with respect to the beam axis. Dashed lines show the background as well as small contaminant peaks. The decay functions yielding the fits displayed in the left part are presented in the middle with their statistical uncertainties. The decay function of the feeding transition of 861 keV is also shown as determined from independent fits at the four detector angles. Its area is normalized to that of the decay function of the 808-keV transition. The τ curves and their statistical uncertainties calculated with the decay functions shown in the middle of the figure are presented on the rhs. The lifetimes τ_{θ} derived at the four detector angles and their statistical errors are also displayed. The final adopted value of the lifetime is $\langle\tau\rangle=190\pm34$ fs.

transitions, for the *S* band and the g.s.b., respectively (cf. Fig. 1). In this way, four line shapes (as observed at the angles of 34.6°, 59.4°, 120.6°, and 145.4°) for each transition of interest were obtained and analyzed independently according to the procedure outlined in details in Refs. [17,18]. Here, we recall only the main points of that procedure. The aim is the determination of the decay function $b_{ij}\lambda_i n_i(t)$ in Eq. (1) as a whole, i.e., of its numerical values as a function of the time *t*. In this way, we consider Eq. (1) as an integral equation for the decay function and describe its solution by a set of second-order polynomials over separate time intervals which are smoothly interconnected at the interval borders. Actually, the line shape analysis consists of varying the number and positions of the time borders (on the *t* scale) until the best χ^2 fit of the line shape (on the E_{γ} scale) is obtained. The correlation matrix of the fit allows for the determination of the statistical uncertainties in all subsequent calculations. In Fig. 3, the procedure is illustrated for the 808-keV transition in the *S* band at the four different detector angles. The fits of the line shapes are displayed on the left-hand side. In the middle,

the decay functions of the transition corresponding to the best fits are presented with their statistical uncertainties.

The line shape analysis yields the decay functions of the level of interest i and of the feeding levels h. When they are determined, lifetime τ can be calculated according to the formalism of the differential decay-curve method (DDCM) [27] presented for the DSAM case in Ref. [17]:

$$\tau_i(t) = \frac{-\lambda_i \int_0^t dt' n_i(t') + \sum_h b_{hi}\lambda_h \int_0^t dt' n_h(t')}{\lambda_i n_i(t)}, \quad (3)$$

where the summation over h includes all direct feeders of level i and automatically takes into account the feeding history. Because lifetime τ is a constant, function $\tau_i(t)$, i.e., the τ curve given by Eq. (3) should represent a straight line when plotted versus time t. Actually, this is realized only within some ''region of sensitivity'' where the values of the numerator and the denominator in Eq. (3) are not too small. Also, due to the polynomial parametrization of the decay functions, the values of the latter are not really reliable for very short and large times t. Lifetime τ is determined as a weighted average of the $\tau_i(t)$ values within the sensitivity region. It should be mentioned that deviations of the τ curve from a constant behavior within the sensitivity region immediately indicate the existence of systematic errors in the analysis. In each of the rings 0, 1, 5, and 6, the line shape analysis and the lifetime determination were performed independently. Since Eq. (3) implies a knowledge of all direct feeders, we also had to investigate the intensity balance at levels of interest. The intensities of the γ rays involved in the analysis were derived using the full statistics matrix which registers coincidences between any pair of detectors of the GASP and the ^{152}Eu efficiency calibration (cf. Sec. II). The different positions of the detector rings with respect to the beam axis nearly ensure a smoothing of the angular correlation of the coincident γ rays, which allows for the derivation of the intensities within a good approximation. Due to the use of gates set on lower-lying transitions, it turned out that some unknown feeding or side feeding is present at every investigated level. Therefore, we adopted an often applied hypothesis on the time behavior of the side feeding, namely, that it is the same as that of the known feeding. In addition, we investigated the influence of side feeding on the results obtained for the lifetimes (cf. below). To apply our hypothesis, the total intensity of the feeding decay functions was renormalized to the intensity of the depopulating decay function and the τ curves were calculated according to Eq. (3). Examples of τ curves obtained for the 808-keV transition in the S band at the four detector angles are shown in Fig. 3, rhs. In the middle of this figure are displayed the decay functions used for the calculation of the τ values. The weighted average values τ_θ within the sensitivity region and their statistical uncertainties $\Delta\tau_\theta$ were calculated using error propagation and taking into account the correlations between the different quantities participating in Eq. (3). The final result for τ was obtained as an unweighted mean of the values determined independently at the different angles (rings). For the uncertainty of its value, we adopted the square root of the variance of the results obtained at the four different rings. We preferred this derivation of the mean value and its uncertainty because it takes better into account the systematic errors of the analysis at the individual rings (see also discussion of a similar problem in Ref. [18]).

The investigation of the uncertainties due to side feeding was done according to the approach outlined in Ref. [18]. For a fixed value of τ, it is possible to solve Eq. (3) with respect to the decay function $D^{sf}(t)$ of the side feeding (sf),

$$D^{sf}(t) = \tau\frac{d}{dt}\lambda_i n_i(t) + \lambda_i n_i(t) - \sum_h b_{hi}^{kf}\lambda_h^{kf} n_h^{kf}(t), \quad (4)$$

where the index kf stands for known feeding. Different assigned values of the lifetime τ lead to different functions $D^{sf}(t)$, which can be inspected for a physically reasonable behavior. In both directions of increasing and decreasing of τ, at some critical τ value, time regions appear where the calculated function $D^{sf}(t)$ is characterized by negative values. Obviously values of τ beyond the critical ones should be excluded. Thus, lower τ_{min} and upper τ_{max} limits for the lifetime can be determined which reflect the uncertainty due to side feeding.

Finally, we have investigated the effect of a possible incomplete knowledge of the stopping powers (SP). For this purpose, we increased and decreased by 10% our basic set of stopping powers and reanalyzed some part of the data. In this way, the corresponding lower τ_{low}^{SP} and upper τ_{up}^{SP} limits for τ were derived which provide an estimate of the related systematic error when compared to the adopted values of the lifetimes.

IV. RESULTS

In the present work, eight lifetimes have been derived, five in the S band and three in the ground-state band. The results of the analysis are summarized in Table II. Examples of fits of line shapes used in the analysis are shown in Figs. 4 and 5. According to the adopted hypothesis on side feeding (cf. above, Sec. III), the difference between the effective lifetimes of two successive levels should yield the lifetime of the lower one. This expectation is realized within the error bars of the lifetimes derived from the line shape analysis (cf. Table II). The fraction of side feeding of the levels under investigation varies from 12% to 41%. The amount of side feeding significantly influences the precision of the derived lifetimes. When its fraction is small (12% at the 22^+ level of the g.s.b.), the uncertainties due to side feeding fall into the error bars of the derived lifetime. When this fraction is large, these uncertainties are well above the adopted error bars of lifetime τ. It is interesting to mention that the limits obtained with a variation of side-feeding in Table II indicate that the deviations towards shorter lifetimes may be quantitatively larger than those towards longer ones. Also, these data help to recognize the lifetimes whose precision depends on the hypothesis involved in the analysis. Concerning the role of the incomplete knowledge of the stopping powers, in almost

TABLE II. Lifetimes determined in the present work. In columns 1 and 2, the energy and spin of the levels investigated are shown, respectively. The depopulating γ-ray transitions whose line shapes were analyzed are displayed in column 3. The deduced effective lifetimes are presented in column 4. The next columns characterize only levels whose lifetimes were determined and not the highest feeding levels used in the analysis. First, the fraction of the side-feeding intensity I_γ^{sf} is displayed. In columns 6 and 7, the lower and upper limits for the lifetime τ are shown, respectively, as derived from the variation of the side feeding (SF). Further, the lower τ_{low}^{SP} and upper τ_{up}^{SP} values of the lifetimes, which can be obtained with 10% increase and reduction of the stopping powers, respectively, are presented. The adopted lifetimes from the present work and their uncertainties are given in the next two columns. Finally, lifetimes taken from Refs. [5], [8] are shown for comparison.

E_{lev}		E_γ	τ_{eff}	I_γ^{sf}	Variation of SF				Adopted		Reference [5]		Reference [8]	
					τ_{min}	τ_{max}	τ_{low}^{SP}	τ_{up}^{SP}	τ	$\Delta\tau$	τ	$\Delta\tau$	τ	$\Delta\tau$
(keV)	I^π	(keV)	(ps)	(%)	(fs)	(fs)	(fs)	(fs)	(fs)	(fs)	(fs)	(fs)	(fs)	(fs)
g.s. band														
4859	20^+	681	1.7	36	140	450	327	396	358	95	330	140		
5572	22^+	714	1.3	12	260	340	268	319	291	52	490	$^{+170}_{-140}$		
6329	24^+	756	1.1	31	120	280	205	245	223	43	490	120		
7130	26^+	802	0.9											
S band														
5320	22^+	685	1.6	20	340	460	352	446	395	84	490	60	460	80
6070	24^+	750	1.2	19	180	320	232	291	259	27	390	200	210	80
6878	26^+	808	1.0	34	65	235	177	207	190	34	230	130	160	50
7739	28^+	861	0.8	41	30	150	113	136	123	25	170	40	160	40
8651	30^+	912	0.7	32	25	130	78	96	86	22	120	20	120	20
9611	32^+	961	0.6											

all cases the uncertainties related to it are within the adopted error bars of the lifetimes.

For comparison, lifetime data from Ref. [5] are also presented in Table II (in the column Ref. [5]). In Ref. [5], these data were obtained as an average of the results of the earlier RDDS [7] and DSAM [8] measurements. The lifetimes derived in the present work are as a rule shorter, although in some cases agreement is observed, mainly due to the large uncertainties of the previous data. On the other hand, our new values for the *S* band are quite close to the results given in Ref. [8], which are also shown in Table II, and the agreement with them is much better. This fact, as well as the smaller uncertainties of our results, shows that the present work significantly contributes to the improvement of the precision of the lifetimes at high spin in ^{156}Dy.

The reduced transition probabilities obtained from the lifetimes derived in the present work are presented in Table III.

V. DISCUSSION

In Fig. 6, we present the $B(E2,I\rightarrow I-2)$ transition strengths determined in the present work within the spin range $I=22\hbar$-$30\hbar$ of the yrast band. The yrast band consists of the levels of the g.s.b. up to the $I^\pi=16^+$ level, where the *S* band becomes energetically favored (cf. Fig. 1). In addition, we show for completeness in Fig. 6 also the $B(E2)$'s derived for the lower-lying yrast states using the data from the accompanying RDDS measurement (cf. Sec. II) and which will be thoroughly discussed in a forthcoming paper [16]. Other available data from Ref. [5] are also displayed. The experimental values are compared to calculations performed in the framework of different nuclear models. The simplest of them is the axially symmetric rigid-rotor model [28] where the intraband $B(E2)$'s are given by the well known formula

$$B(E2,I\rightarrow I-2)=\frac{5}{16\pi}Q_0^2\langle IK20|I-2K\rangle^2 \tag{5}$$

with an intrinsic quadrupole moment Q_0 related [29] to deformation β via

$$Q_0=\frac{3}{\sqrt{5\pi}}ZR_0^2\beta(1+0.16\beta). \tag{6}$$

According to Ref. [30], due to the difference between the nuclear charge distribution and the mean field, $\beta \approx 1.1\beta_{mean\ field}$. Quantity Q_0, which should be a constant for all band members, is usually determined from the data using Eq. (5) and the transition strength at the bottom of the rotational band. From the half life $T_{1/2}=0.823(7)$ of the 2_1^+ level of the ground-state band given in Ref. [5], one can derive the transition strength $B(E2,2_1^+\rightarrow 0_1^+)=0.744(19)e^2\,\mathrm{b}^2$ and $Q_0=6.12(8)e$. With the latter value, the $B(E2)$'s for the higher-lying transitions were recalculated, again assuming $K=0$, and are presented in Fig. 6 with the solid line A. Apart from some fluctuations and the expected failure at the band-crossing point ($I^\pi=16^+$), the agreement with the data is impressive and indicates similar quadrupole deformations of the g.s.b. and the *S* band at low and high spins, respectively. Thus, the conclusions for rotation-induced shape changes [7] in the spin region below

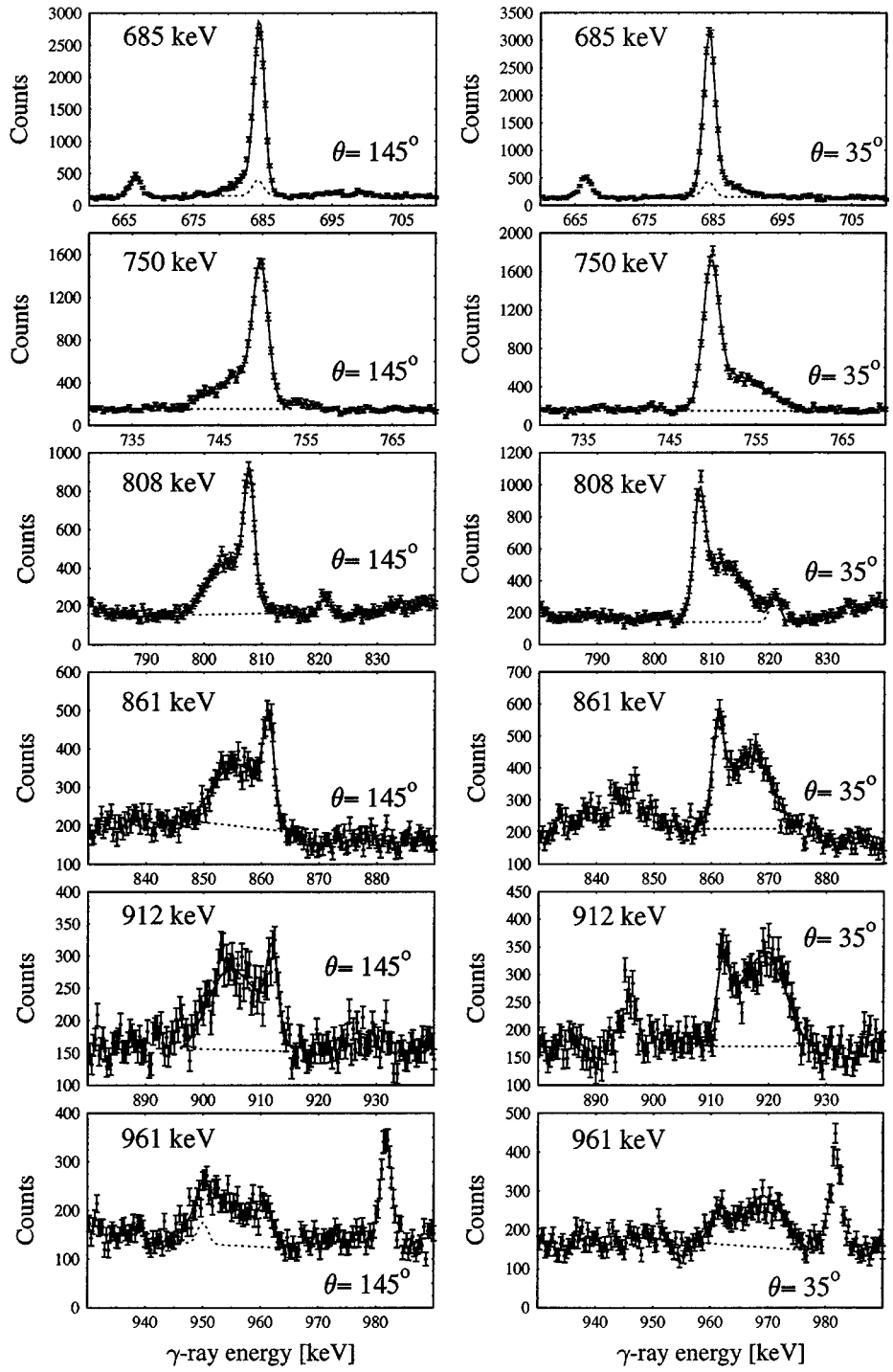

FIG. 4. Fitted line shapes of transitions in the *S* band observed at 35° and 145°. The background and contaminants present are also displayed with dashed lines.

$I=30\hbar$, based on earlier data, are not supported by the present work. However, we cannot exclude the possible reduction of the yrast $B(E2)$'s at higher spin ($I\approx 38\hbar$) observed in Ref. [8] and associated with band termination and a gradual transition towards noncollective oblate shape [2]. It is interesting to note that the recent [31] data on the lifetimes of the yrast states in the neighboring nucleus ^{158}Er indicate a behavior of the B(E2) transition strengths which only slightly differs from that observed in ^{156}Dy in the present work. In ^{158}Er, the data support some small reduction of the collectivity after the band-crossing.

Of course, a rigid-rotor-like behavior of the transition strengths does not necessarily mean that the average values of the shape variables β and γ remain stable. It might be that they change in a correlated way, leading to the observed features. However, the detailed investigation of such effects is beyond the scope of the present work. Instead, we considered other available theoretical calculations based on more sophisticated approaches than the axially symmetric rigid-rotor model and compare some of them to the data in Fig. 6, referring the reader for more details to the quoted works. Many theoretical efforts have been devoted to the description

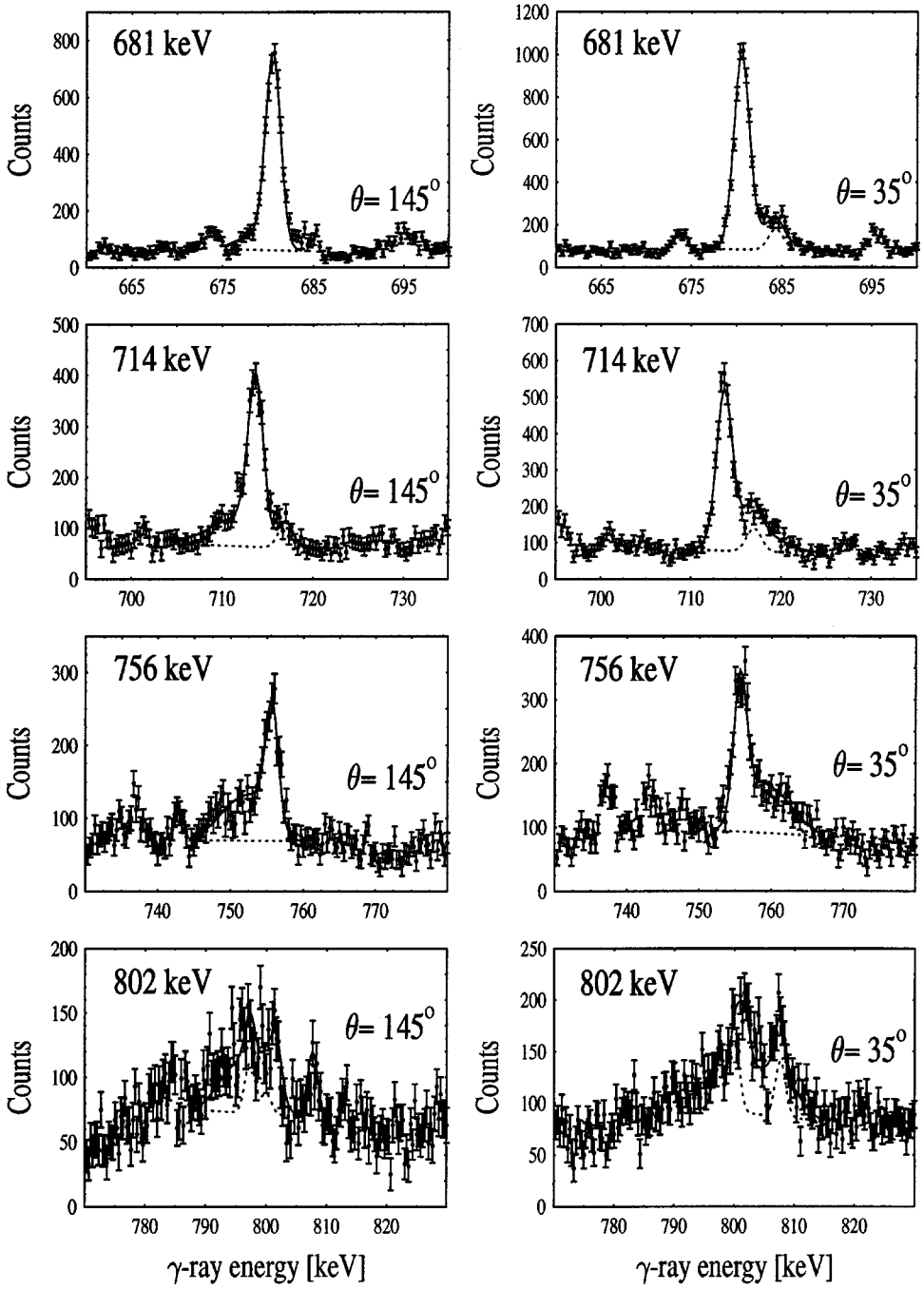

FIG. 5. Same as in Fig. 4, but for the ground-state band.

of the electromagnetic transition strengths between the yrast states in ^{156}Dy. Bhatt *et al.* [32] have recently investigated the wave functions of the yrast states of even-even nuclei, and, in particular, of ^{156}Dy, in terms of quadrupole collective states of nucleons occupying normal and abnormal parity orbitals. This work predicts yrast $B(E2)$ values similar to those of a symmetric rigid rotor, but with a trend for a reduction of the collectivity with increasing spin after $I^{\pi}=20^{+}$. Cranked Hartree-Fock-Bogoliubov calculations with variation after exact projection onto a good particle number [10] give an overall description of the level energies and also predict a behavior of the $B(E2)$ values, which is very close to the expectations for a symmetric rigid rotor. However, as the authors point out, the calculation cannot reproduce the fine structure of the $B(E2)$ data, and especially the fluctuations around the band-crossing region. The projected shell-model approach applied in Ref. [12] can only roughly describe the present data. The best agreement between experiment and semimicroscopic calculations is provided by the work of Sun and Egido [11]. They used an angular momentum–projected Tamm-Dancoff approximation including two- and four-quasiparticle states. The calculated values of the $B(E2)$'s in Ref. [11] are presented in Fig. 6 with line B. Algebraic approaches within the framework of the IBM have also been tried to describe the yrast states. Thus, Heyde *et al.* [33,34] included core-excitations yielding complementary bosons which shift to higher spins the so called cutoff of the yrast $B(E2)$'s. Also, Chuu and Hsieh [35] applied the

TABLE III. Reduced electromagnetic transition probabilities $B(E2)$ derived in this work. In column 1, the band investigated is displayed. The level and depopulating transition energies are shown (in keV) in the next two columns followed by the spin/parity of the initial (I_i^π) and final (I_f^π) levels. The last column presents the $B(E2)$ data in Weisskopf units. Uncertainties are shown in brackets.

Band	E_{lev}	E_γ	I_i^π	I_f^π	$B(E2)$ (e^2 b^2)	$B(E2)$ (W.u.)
g.s. band	4859	681	20^+	18^+	1.547 (410)	310 (82)
	5572	714	22^+	20^+	1.502 (268)	301 (54)
	6329	756	24^+	22^+	1.477 (285)	296 (57)
S band	5320	685	22^+	20^+	1.364 (290)	274 (58)
	6070	750	24^+	22^+	1.321 (138)	265 (28)
	6878	808	26^+	24^+	1.243 (222)	249 (45)
	7739	861	28^+	26^+	1.397 (284)	280 (57)
	8651	912	30^+	28^+	1.499 (383)	300 (77)

IBM with two-quasiparticle states to describe the structure of even-even Dy nuclei. The results of these two IBM calculations are presented in Fig. 6 with lines C and D, respectively. They can only very roughly describe the experimental data in the spin region $I>20\hbar$ measured in the present work.

Thus, we can conclude that our study confirms the calculations made earlier within semimicroscopic mean-field approaches [10–12,32], which predict no change or only a marginal decrease of the collectivity in the spin region $I=20\hbar-30\hbar$ of the yrast band of ^{156}Dy. This is consistent also with the calculations of Dudek and Nazarewicz [36] who applied the generalized Strutinsky-cranking method to investigate the shape evolution of transitional nuclei at high spin. According to that work, at spin $I=30\hbar$, ^{156}Dy is characterized by a nuclear shape which is close to prolate, with a deformation of $\beta_{mean\ field}=0.23$. This deformation is only a bit smaller than the value of 0.255(4), which can be extracted from the $B(E2,2_1^+\rightarrow 0_1^+)$ transition strength.

Finally, we would like to mention the slightly higher collectivity of the transitions belonging to the continuation of the g.s.b compared to that of the transitions along the *S* band (cf. Table III). Although the effect is within the error bars of the data, it would be interesting to verify it by refined theoretical calculations in the future.

VI. SUMMARY AND CONCLUSIONS

By means of the Doppler-shift attenuation method, lifetime measurements in ^{156}Dy were performed using the multidetector array GASP. The data were analyzed according to the differential decay-curve method and eight lifetimes of excited nuclear states were derived in the *S* band and the ground-state band of that nucleus. These new lifetime values significantly improve the precision of the knowledge of the properties of the high-spin states considered. Along the yrast band, the behavior of the reduced transition probabilities $B(E2)$ is consistent with a rigid-rotor description and earlier suggestions for rotation-induced shape changes are not confirmed. The present data supports calculations within semimicroscopic mean-field approaches [10–12,32] which also predict no change or only a marginal decrease of the collectivity in the spin region $I=20\hbar-30\hbar$ of the yrast band of ^{156}Dy and give results similar to those of the rigid-rotor model.

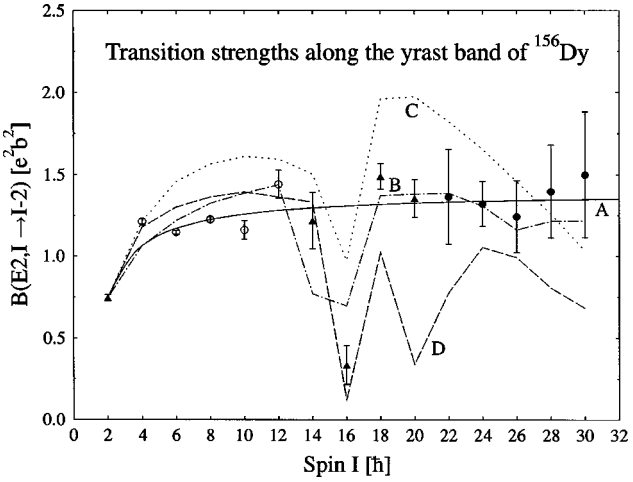

FIG. 6. $B(E2)$ transition strengths in the yrast band of ^{156}Dy. The measured values are compared to the expected ones for a rigid rotor (line *A*) and to calculations from Refs. [11,34,35], presented by the lines *B*,*C*, and *D*, respectively. For the spin region $I=22\hbar-30\hbar$, the experimental data are taken from the present work. At lower spins, data from Ref. [16] are shown with open circles, while the data taken from Ref. [5] are shown with triangles.

ACKNOWLEDGMENTS

This work was supported by the BMBF (Germany) under Contract No. HPRI-CT-1999-00083 and by the European Union TMR Programme under Contract No. 06K-167. One of us (P.P.) would like to thank the colleagues from the University of Cologne for their kind hospitality and to acknowledge the support provided by the Bulgarian National Research Foundation (BNRF).

[1] M.A. Riley, J. Simpson, J.F. Sharpey-Schafer, J.P. Cresswell, H.W. Cranmer-Gordon, P.D. Forsyth, D. Howe, A.H. Nelson, P.J. Nolan, P.J. Smith, N.J. Ward, J.C. Lisle, E. Paul, and P.M. Walker, Nucl. Phys. **A486**, 456 (1988).

[2] F.G. Kondev, M.A. Riley, R.V.F. Janssens, J. Simpson, A.V. Afanasjev, I. Ragnarsson, I. Ahmad, D.J. Blumenthal, T.B. Brown, M.P. Carpenter, P. Fallon, S.M. Fischer, G. Hackman, D.J. Hartley, C.A. Kalfas, T.L. Khoo, T. Lauritsen, W.C. Ma, D. Nisius, J.F. Sharpey-Schafer, and P.G. Varmette, Phys. Lett. B **437**, 35 (1998).

[3] H.R. Andrews, D. Ward, R.L. Graham, and J.S. Geiger, Nucl. Phys. **A219**, 141 (1974).
[4] R.M. Lieder, H. Beuscher, W.F. Davidson, A. Neskakis, C. Mayer-Böricke, Y. El Masri, P. Monseu, J. Steyart, and J. Vervier, Phys. Lett. **49B**, 161 (1974).
[5] R.G. Helmer, Nucl. Data Sheets **65**, 65 (1992).
[6] D. Ward, H.R. Andrews, O. Häusser, Y. El Masri, M.M. Aléonard, I. Yang-Lee, R.M. Diamond, F.S. Stephens, and P.A. Butler, Nucl. Phys. **A332**, 433 (1979).
[7] H. Emling, E. Grosse, R. Kulessa, D. Schwalm, and H.J. Wollersheim, Nucl. Phys. **A419**, 187 (1984).
[8] H. Emling, I. Ahmad, P.J. Daly, B.K. Dichter, M. Drigert, U. Garg, Z.W. Grabowski, R. Holzmann, R.V.F. Janssens, T.L. Khoo, W.C. Ma, M. Piiparinen, M.A. Quader, I. Ragnarsson, and W.H. Trzaska, Phys. Lett. B **217**, 33 (1989).
[9] T.K. Alexander and J.S. Forster, Adv. Nucl. Phys. **10**, 197 (1978).
[10] M.L. Cescato, Y. Sun, and P. Ring, Nucl. Phys. **A533**, 455 (1991).
[11] Y. Sun, and J.L. Egido, Nucl. Phys. **A580**, 1 (1994)
[12] V. Velazquez, J.G. Hirsch, Y. Sun, and M.W. Guidry, Nucl. Phys. **A653**, 355 (1999).
[13] D. Bazzacco, Chalk River Report No. (AECL 10613), p. 386.
[14] P. Petkov, D. Tonev, J. Gableske, A. Dewald, and P. von Brentano, Nucl. Instrum. Methods Phys. Res. A **437**, 274 (1999).
[15] P. Petkov, D. Tonev, A. Dewald, and P. von Brentano, Nucl. Instrum. Methods Phys. Res. A **488**, 555 (2002).
[16] O. Möller *et al.* (unpublished).
[17] G. Böhm, A. Dewald, P. Petkov, and P. von Brentano, Nucl. Instrum. Methods Phys. Res. A **329**, 428 (1993).
[18] P. Petkov, J. Gableske, O. Vogel, A. Dewald, P. von Brentano, R. Krücken, R. Peusquens, N. Nicolay, A. Gizon, J. Gizon, D. Bazzacco, C. Rossi-Alvarez, S. Lunardi, P. Pavan, D.R. Napoli, W. Andrejtscheff, and R.V. Jolos, Nucl. Phys. **A640**, 293 (1998).
[19] G. Winter, ZfK Rossendorf Report ZfK-497, 1983 (unpublished).
[20] G. Winter, Nucl. Instrum. Methods Phys. Res. **214**, 537 (1983).
[21] W.M. Currie, Nucl. Instrum. Methods **73**, 173 (1969).
[22] J. Lindhard, M. Scharff, and H.E. Schiøtt, K. Dan. Vidensk. Selsk. Mat. Fys. Medd. **33**, 14 (1963).
[23] L.C. Northcliffe and R.F. Schilling, Nucl. Data Tables **7**, 233 (1970).
[24] J. F. Ziegler and J. P. Biersack, in *Treatise on Heavy-Ion Science*, edited by D. A. Bromley (Plenum Press, New York, 1985), Vol. 6, p. 95.
[25] J.F. Ziegler and W.K. Chu, At. Data Nucl. Data Tables **13**, 463 (1974).
[26] J. Keinonen, in *Capture Gamma-Ray Spectroscopy and Related Topics–1984*, edited by S. Raman, AIP Conf. Proc. No. **125** (AIP, New York, 1985), p. 557.
[27] A. Dewald, S. Harissopulos, and P. von Brentano, Z. Phys. A **334**, 163 (1989).
[28] A. Bohr and B. R. Mottelson, Nuclear Structure (Benjamin, New York, 1975), Vol. 2.
[29] A. Bohr and B.R. Mottelson, K. Dan. Vidensk. Selsk. Mat. Fys. Medd. **30**, 1 (1955).
[30] W. Nazarewicz, M.A. Riley, and J.D. Garrett, Nucl. Phys. **A512**, 61 (1990).
[31] S.L. Shepherd, J. Simpson, A. Dewald, P. Petkov, P.J. Nolan, M.A. Riley, A.J. Boston, T.B. Brown, R.M. Clark, P. Fallon, D.J. Hartley, S. Kasemann, R. Krücken, P. von Brentano, R.W. Laird, E.S. Paul, and R. Peusquens, Phys. Rev. C **65**, 034320 (2002).
[32] K.H. Bhatt, S. Kahane and S. Raman, Phys. Rev. C **61**, 034317 (2000).
[33] K. Heyde, P. Van Isacker, J. Jolie, J. Moreau, and M. Waroquier, Phys. Lett. **132B**, 15 (1983).
[34] K. Heyde, J. Jolie, P. Van Isacker, J. Moreau, and M. Waroquier, Phys. Rev. C **29**, 1428 (1984).
[35] D.S. Chuu and S.T. Hsieh, Phys. Rev. C **38**, 960 (1988).
[36] J. Dudek and W. Nazarewicz, Phys. Rev. C **31**, 298 (1985).